

An analytical model for the history of cosmic star formation

Lars Hernquist^{1*} and Volker Springel^{2‡}

¹*Harvard-Smithsonian Center for Astrophysics, 60 Garden Street, Cambridge, MA 02138, USA*

²*Max-Planck-Institut für Astrophysik, Karl-Schwarzschild-Straße 1, 85740 Garching bei München, Germany*

7 November 2018

ABSTRACT

We use simple analytic reasoning to identify physical processes that drive the evolution of the cosmic star formation rate, $\dot{\rho}_*$, in cold dark matter universes. Based on our analysis, we formulate a model to characterise the redshift dependence of $\dot{\rho}_*$ and compare it to results obtained from a set of hydrodynamic simulations which include star formation and feedback.

We find that the cosmic star formation rate is described by two regimes. At early times, densities are sufficiently high and cooling times sufficiently short that abundant quantities of star-forming gas are present in all dark matter halos that can cool by atomic processes. Consequently, $\dot{\rho}_*$ generically rises exponentially as z decreases, independent of the details of the physical model for star formation, but dependent on the normalisation and shape of the cosmological power spectrum. This part of the evolution is dominated by gravitationally driven growth of the halo mass function. At low redshifts, densities decline as the universe expands to the point that cooling is inhibited, limiting the amount of star-forming gas available. We find that in this regime the star formation rate scales approximately as $\dot{\rho}_* \propto H(z)^{4/3}$, in proportion to the cooling rate within halos.

We demonstrate that the existence of these two regimes leads to a peak in the star formation rate at an intermediate redshift $z = z_{\text{peak}}$. We discuss how the location of this peak depends on our model parameters. Only star formation efficiencies that are unrealistically low would delay the peak to $z \simeq 3$ or below, and we show that the peak cannot occur above a limiting redshift of $z \approx 8.7$. For the star formation efficiency adopted in our numerical simulations, $z_{\text{peak}} \approx 5 - 6$.

We derive analytic expressions for the full star formation history and show that they match our simulation results to better than $\simeq 10\%$. Using various approximations, we reduce the expressions to a simple analytic fitting function for $\dot{\rho}_*$ that can be used to compute global cosmological quantities that are directly related to the star formation history. As examples, we consider the integrated stellar density, the supernova and gamma-ray burst (GRB) rates observable on Earth, the metal enrichment history of the Universe, and the density of compact objects. We also briefly discuss the expected dependence of the star formation history on cosmological parameters and the physics of the gas.

Key words: cosmology: theory – galaxies: formation – methods: analytical.

1 INTRODUCTION

The history of cosmic star formation is of fundamental importance to cosmology, not only to galaxy formation itself,

but also for ongoing efforts to determine cosmological parameters and the matter content of the Universe. Over the past decade, various attempts have been made to directly map out the evolution of star formation observationally (e.g. Gallego et al., 1995; Madau et al., 1996, 1998; Lilly et al., 1996; Cowie et al., 1996, 1999; Connolly et al., 1997; Hughes et al., 1998; Treyer et al., 1998; Tresse & Maddox, 1998; Pas-

* E-mail: lars@cfa.harvard.edu

‡ E-mail: volker@mpa-garching.mpg.de

carelle et al., 1998; Steidel et al., 1999; Flores et al., 1999; Gronwall, 1999; Hogg, 2001; Baldry et al., 2002; Lanzetta et al., 2002; Wilson et al., 2002). Obtaining precise measurements of the star formation rate density, $\dot{\rho}_*$, is made challenging, however, by the difficult nature of these observations and also by uncertainties in systematic effects such as dust extinction. Partly for this reason, there is strong motivation for predicting $\dot{\rho}_*$ theoretically to provide a framework for interpreting the data.

Various theoretical efforts have been made to calculate $\dot{\rho}_*$, using either semi-analytic models (White & Frenk, 1991; Cole et al., 1994; Baugh et al., 1998; Somerville et al., 2001), or numerical simulations (Weinberg et al., 1999; Pearce et al., 2001; Nagamine et al., 2000, 2001; Ascasibar et al., 2002). Unfortunately, due to the complexity of the physics underlying galaxy formation, the predicted behaviour for $\dot{\rho}_*(z)$ can be quite sensitive to the model adopted to describe star formation and associated feedback processes. Perhaps because of this difficulty, there have been few attempts to determine whether some aspects of the expected evolution of the star formation density in cold dark matter cosmologies are relatively insensitive to the details of the physics of star formation. If such a “generic” behaviour exists within a reasonably broad class of physical models, it should be possible to make robust predictions for the shape of the star formation history in cold dark matter universes that could be confronted with observations to test the currently favoured paradigm of hierarchical galaxy formation.

In this paper, we examine this issue in detail. We are motivated by the numerical results presented in Springel & Hernquist (2002b), where we used a large set of hydrodynamic simulations to infer the evolution of the cosmic star formation rate density from high redshift to the present. These simulations included a novel description for star formation and feedback processes within the interstellar medium (Springel & Hernquist, 2002a) and a novel formulation of the equations of motion (Springel & Hernquist, 2002c). The broad range of scales encompassed by our set of simulations, together with extensive convergence tests, enabled us to obtain a converged prediction for $\dot{\rho}_*(z)$ within this model for galaxy formation.

The cosmic star formation history we inferred peaks at a redshift $z_{\text{peak}} \sim 5.5$, declining roughly exponentially towards both low and high redshift. Here, we establish a physical basis for the particular form of the star formation history predicted by our simulations. This makes it possible to arrive at a clearer understanding of the physics that drives the evolution of the cosmic star formation history, and allows us to justify specific analytic fitting functions for the full star formation history. Such closed-form descriptions are particularly useful for computing derived quantities that directly depend on the star formation history and for relating theoretical predictions to observations.

This paper is organised as follows. In Section 2, we present our analytic fitting function for the cosmic star formation history, followed in Section 3 by a detailed analysis of the physical basis for this particular functional form. In Section 4, we then compute a number of derived quantities based on the star formation history. We briefly discuss the expected dependence on cosmological parameters and possible effects of metal enrichment in Section 5, and, finally, we summarise and conclude in Section 6.

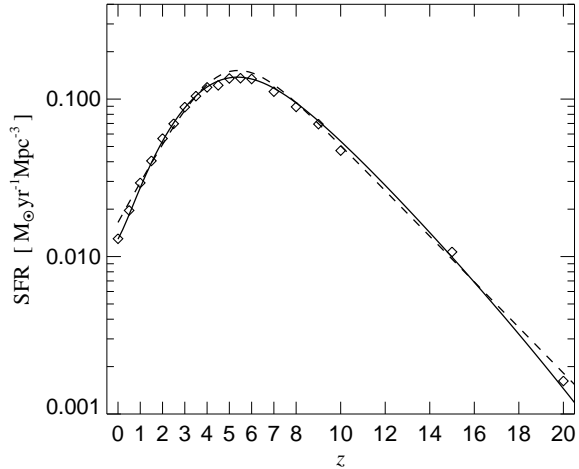


Figure 1. Simulation results for the cosmic star formation history (symbols) compared to different analytic fitting functions. The solid line shows equation (2), while the dashed line gives equation (1), the fitting function originally proposed by Springel & Hernquist (2002b).

2 AN ANALYTIC FIT TO THE COSMIC STAR FORMATION HISTORY

In Springel & Hernquist (2002b), we used a set of numerical simulations to study the evolution of the cosmic star formation rate density from high redshift to the present. To summarise our results compactly, we fitted $\dot{\rho}_*(z)$ using a simple double-exponential function of the form

$$\dot{\rho}_*(z) = \epsilon_* \frac{b \exp[a(z - z_m)]}{b - a + a \exp[b(z - z_m)]}, \quad (1)$$

with $a = 3/5$, $b = 14/15$, $z_m = 5.4$, and $\epsilon_* = 0.15 \text{ M}_\odot \text{ yr}^{-1} \text{ Mpc}^{-3}$. (Our notation here differs slightly from Springel & Hernquist 2002b to avoid confusion with what follows.) This functional form was chosen based purely on the suggestive shape of our numerical result. However, we also suspected that there should be a clear physical basis for the shape of the star formation history, which we did not address. With such a basis, it should be possible to arrive at an appropriate analytic fitting function directly, making it unnecessary to “guess” a particular form for it.

As White & Frenk (1991) have demonstrated, the low-redshift behaviour of the star formation history should be related to the declining efficiency of gas cooling at low redshift, which in itself is caused by the decrease of the mean density of the universe. This effect should hence give rise to a scaling that is related to the expansion rate of the Universe, as measured by the evolution of the Hubble constant. Indeed, for low redshifts, we find empirically that a dependence of the form $\dot{\rho}_* \sim H(z)^{4/3}$ matches our measurements for our model of star formation and feedback very well.

On the other hand, at high redshifts, we clearly see a trend that is close to an exponential. In fact, $\dot{\rho}_* \sim \exp(-z/3)$ provides an acceptable fit to our simulation results, at least over the limited redshift range probed by our calculations. This exponential behaviour is presumably related to the

growth of the halo mass function, which exhibits an exponential cut-off for large masses.

Based on a more thorough study of these ideas, which will be discussed in detail below, an improved fit of the form

$$\dot{\rho}_* = \dot{\rho}_*(0) \frac{\chi^2}{1 + \alpha(\chi - 1)^3 \exp(\beta\chi^{7/4})} \quad (2)$$

can be obtained. Here, the redshift evolution of $\dot{\rho}_*$ is conveniently captured by defining the abbreviation

$$\chi(z) \equiv \left[\frac{H(z)}{H_0} \right]^{\frac{2}{3}}, \quad (3)$$

and where $\alpha = 0.012$, $\beta = 0.041$, and $\dot{\rho}_*(0) = 0.013 \text{ M}_\odot \text{ yr}^{-1} \text{ Mpc}^{-1}$ are introduced as fitting parameters. We find that equation (2) provides an excellent fit to our simulations, and, in particular, is better than equation (1). This is seen in Figure 1, where we compare equations (1) and (2) to our composite simulation result.

At low redshift, we see that equation (2) reduces to $\dot{\rho}_* \propto H(z)^{4/3}$, while the origin of the high-redshift scaling $\dot{\rho}_* \propto \chi^{-1} \exp(-\beta\chi^{7/4})$ that we adopted in our fitting function, is not immediately obvious. In fact, we have chosen this form based on a detailed analytic argument which we will present in the next section. This will also elucidate the dependence of the shape of the star formation history on cosmological parameters, and on the physics of star formation and feedback.

3 PHYSICAL BASIS FOR THE COSMIC STAR FORMATION HISTORY

3.1 Basic equations

Provided that star formation occurs only in dark matter halos, we can compute the cosmic star formation rate density as an integral over the multiplicity function of halos, $g(M, z)$, multiplied by the average normalised star formation rate $s(M, z) = \langle \dot{M}_* \rangle / M$ of halos of a given mass M . This can be written as

$$\dot{\rho}_*(z) = \bar{\rho}_0 \int g(M, z) s(M, z) d \log M, \quad (4)$$

where we term the integrand the ‘‘multiplicity function of star formation’’ (Springel & Hernquist, 2002b) and where $\bar{\rho}_0 \equiv 3\Omega_0 H_0^2 / (8\pi G)$.

The halo multiplicity function $g(M, z)$ can be defined as

$$g(M, z) = \frac{dF}{d \log M}, \quad (5)$$

where $F(M, z)$ is the fraction of mass bound in halos less massive than M . Often, $F(M, z)$ is approximated by the Press & Schechter (1974) mass function, which is known to provide a reasonable parameterisation of the evolution of halo abundance in CDM cosmologies. The Press-Schechter mass function can be written as

$$F(M, z) = \text{erf} \left[\frac{\delta_c}{\sqrt{2} \sigma(M, z)} \right], \quad (6)$$

where the function $\sigma(M, z)$ describes the linearly extrapolated rms-fluctuations in top-hat spheres of size equal to an

enclosed background mass M . For the threshold parameter δ_c , we adopt the canonical value $\delta_c = 1.686$.

Recent studies have shown that there are slight deviations between the Press-Schechter mass function with the results of high-resolution collisionless simulations of structure formation, particularly at high mass-scales, and around the exponential turn-off. However, Sheth & Tormen (1999, 2002) have derived an improved parameterisation of the mass function by generalising the excursion set formalism to allow for ellipsoidal collapse. We can rewrite their result in an integrated form as

$$F(M, z) = A \left[\text{erf} \left(\frac{\sqrt{a} \delta_c}{\sqrt{2} \sigma} \right) + \frac{1}{\sqrt{2^{3/5} \pi}} \tilde{\Gamma} \left(\frac{1}{5}, \frac{a \delta_c^2}{2 \sigma^2} \right) \right], \quad (7)$$

where $a = 0.707$, $A = [1 + \Gamma(1/5) / \sqrt{2^{3/5} \pi}]^{-1} = 0.3222$, and $\tilde{\Gamma}$ is the lower incomplete gamma function,

$$\tilde{\Gamma}(a, x) = \int_0^x t^{a-1} \exp(-t) dt. \quad (8)$$

The Sheth & Tormen mass function has been tested over a large dynamic range in mass and provides an accurate description of numerical results (Jenkins et al. 2001). In what follows, we prefer the Sheth & Tormen mass function for this reason, but will also employ the Press-Schechter form for comparison and because it works very well at high redshift (Jang-Condell & Hernquist, 2001).

The evolution of $\sigma(M, z)$ determines the evolution of the mass function. In linear theory, we have

$$\sigma^2(M, z) = D^2(z) \int_0^\infty \frac{dk}{2\pi^2} k^2 P(k) \left[\frac{3j_1(kR)}{kR} \right]^2, \quad (9)$$

where $D(z)$ is the linear growth factor, normalised to unity at the present time, and $P(k)$ is the linear power spectrum. The growth factor $D(z)$ can be computed from

$$D(z) = D_0 H(z) \int_z^\infty \frac{(1+z') dz'}{H^3(z')}, \quad (10)$$

using the Hubble constant

$$H(z) = H_0 \left[\Omega_m (1+z)^3 + (1 - \Omega_m - \Omega_\Lambda) (1+z)^2 + \Omega_\Lambda \right]^{1/2}$$

and adjusting the normalisation constant D_0 such that $D(0) = 1$.

For the purposes of this analysis, we define halos of virial mass M to be spheres of radius R that enclose a characteristic overdensity of 200 with respect to the *critical density*. For each halo, we define a virial velocity

$$V_{\text{vir}}^2 \equiv \frac{GM}{R}. \quad (11)$$

We can then express the mass and virial radius as

$$M = \frac{V_{\text{vir}}^3}{10GH(z)}, \quad R = \frac{V_{\text{vir}}}{10H(z)}. \quad (12)$$

We further define the halo’s virial temperature as

$$T_{\text{vir}} = \frac{\mu}{2k} V_{\text{vir}}^2 \simeq 36 \text{ K} \left(\frac{V_{\text{vir}}}{\text{km s}^{-1}} \right)^2, \quad (13)$$

where $\mu \simeq 0.6 m_p$ is the mean molecular weight. Note that T_{vir} is a function only of circular velocity. The virial temperature of a halo of given mass M at redshift z is hence given by

$$T(M, z) = 9.5 \times 10^7 \text{ K} \left(\frac{M}{10^{15} h^{-1} M_\odot} \right)^{\frac{2}{3}} \chi(z), \quad (14)$$

where $\chi(z)$ is defined in equation (3).

3.2 A model for the star formation efficiency

Given that the Sheth & Tormen mass function specifies $g(M, z)$ unambiguously, it is clear that the key for an explanation of the full star formation history lies in an understanding of the evolution of the normalised star formation rate $s(M, z)$. In Springel & Hernquist (2002b), we measured $s(M, z)$ directly at different epochs from our set of hydrodynamic simulations. We found that only halos with virial temperatures above $\simeq 10^4$ K formed any stars, which is simply caused by the inefficiency of atomic line cooling at lower temperatures, when metals and molecular cooling are neglected. While molecular cooling might be of high importance for the formation of the very first stars in the high-redshift universe, it should be largely unimportant for the formation of the bulk of the stars. On the other hand, metal line cooling may boost the cooling rates in halos at late times, provided their diffuse gas becomes significantly enriched with heavy elements. In section 5.2, we will discuss separately to what extent our neglect of metal cooling could influence our results.

From our simulations, we further found that the normalised star formation rate, expressed as a function of virial temperature, has approximately the same shape at different redshifts, differing only in amplitude. This can be expressed formally by defining a function

$$\tilde{s}(T) \equiv s[M(T, z), z], \quad \text{at } z=0, \quad (15)$$

where $M(T, z)$ is the mass of a halo of virial temperature T at redshift z . The inference of the near shape invariance of $s(M, z)$ when expressed as a function of virial temperature then allows us to make the ansatz

$$s(M, z) = \tilde{s}[T(M, z)]q(z), \quad (16)$$

where $q(z)$ describes the scaling of the normalised star formation rate with redshift, and $T(M, z)$ is given by equation (14). We note that in different models for the physics of star formation and feedback it may not be possible to factorise the star formation rate in the form of equation (16). However, we expect this ansatz to work for models that are broadly similar to the one considered in our simulations.

Schematically, $\tilde{s}(T)$ vanishes for temperatures below 10^4 K. For higher temperatures, it assumes a roughly constant value of $\tilde{s}(T) \simeq s_0$, up to $T \approx 10^6$ K, where it begins to rise by about a factor of 3 towards a maximum reached around 10^7 K, beyond which $\tilde{s}(T)$ starts to fall again towards higher temperatures. The detailed shape of $\tilde{s}(T)$ is in part related to the strong feedback by galactic winds considered in our simulations. These winds are an important mechanism for maintaining the normalised star formation rate at a relatively low level in small halos within the temperature range $10^4 - 10^6$ K. Likewise, the scale at which the normalised star formation rate starts to increase is related to the speed of the winds. When they are no longer able to escape from halos, the winds lose their ability to suppress star formation.

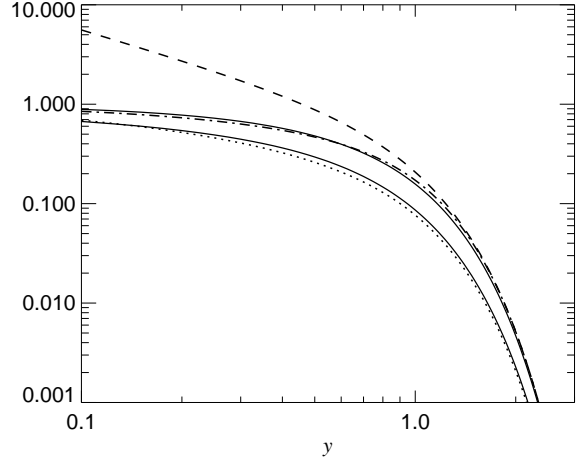


Figure 2. Different approximations for the mass fraction above star formation threshold. The upper solid line shows the exact value of $1 - \text{erf}(y)$. The dashed line is the approximation based on equation (21), while the dot-dashed line shows the approximation (22). Similarly, the lower solid line and the dotted line compare the corresponding exact expression for the Sheth & Tormen mass function with our approximation, respectively, as given in equation (23).

We note that perhaps one of the most crucial characteristics of $\tilde{s}(T)$ is its *threshold behaviour*: Below a critical temperature of $T_4 \equiv 10^4$ K, there is no star formation, while above T_4 , the value of $\tilde{s}(T)$ varies only relatively weakly with temperature. Perhaps the simplest reasonable model for the normalised star formation rate therefore takes the form of a step-function:

$$s(M, z) = \tilde{s}(T)q(z) = \begin{cases} s_0 q(z) & \text{for } T > 10^4 \text{ K,} \\ 0 & \text{otherwise.} \end{cases} \quad (17)$$

If we define $M_4(z)$ to be the mass corresponding to a virial temperature of 10^4 K at redshift z , this model immediately implies

$$\dot{\rho}_*(z) = \bar{\rho}_0 s_0 q(z) [F(\infty, z) - F(M_4, z)]. \quad (18)$$

Using the Press-Schechter mass function, this becomes

$$\dot{\rho}_*(z) = \bar{\rho}_0 s_0 q(z) \left[1 - \text{erf} \left(\frac{\delta_c}{\sqrt{2} \sigma_4} \right) \right], \quad (19)$$

where we have introduced $\sigma_4(z) \equiv \sigma[M_4(z), z]$ to describe the rms-fluctuations on the mass scale of the 10^4 K halos. If instead the Sheth & Tormen mass function is used, we obtain

$$\dot{\rho}_*(z) = \bar{\rho}_0 s_0 q(z) \left[1 - A \text{erf} \left(\frac{\sqrt{a} \delta_c}{\sqrt{2} \sigma_4} \right) - \frac{A}{\sqrt{2^{3/5} \pi}} \tilde{\Gamma} \left(\frac{1}{5}, \frac{a \delta_c^2}{2 \sigma_4^2} \right) \right]. \quad (20)$$

At high redshift, we expect the arguments of the error functions in equations (19) and (20), respectively, to be large compared to unity. We can then use an asymptotic expansion of the error function (e.g. Gradstein & Ryshik, 1981) to obtain simpler approximate expressions. To lowest order we have

$$1 - \text{erf}(y) \simeq \frac{1}{\sqrt{\pi}} \frac{\exp(-y^2)}{y}. \quad (21)$$

This approximation is very accurate for $y \gg 1$, and is even reasonable for $y \sim 1$. For $y > 2$, the error is less than 10%, but it grows to 30% for $y \simeq 1$, reaching a factor of 2 for $y \simeq 0.45$. However, because the values of y we encounter in equations (19) and (20), respectively, drop to about 0.2 for $z = 0$, we desire a more accurate approximation at low z . In fact, we propose that

$$1 - \text{erf}(y) \simeq \frac{1}{1 + \sqrt{\pi} y \exp(y^2)} \quad (22)$$

fulfills our requirements very well. This approximation is accurate to better than 12% for all $y \geq 0$. In Figure 2, we compare the approximations (21) and (22) to the exact result. Also shown is the relevant expression for the Sheth & Tormen mass function, where we find that the approximation

$$1 - A \text{erf}(y) - \frac{A}{\sqrt{2^{3/5}\pi}} \tilde{\Gamma}\left(\frac{1}{5}, y^2\right) \simeq \frac{1}{1 + \frac{5}{2}\sqrt{\pi} y \exp(y^2)} \quad (23)$$

provides a similarly small error.

At high redshift, when $\sigma_4(z)$ is small, we hence expect the star formation rate from the Sheth & Tormen mass function to scale as

$$\dot{\rho}_*(z) \propto q(z) \sigma_4(z) \exp\left[-\frac{a\delta_c^2}{2\sigma_4^2}\right]. \quad (24)$$

In the case of the Press-Schechter form, the numerical factor $a = 0.707$ in the argument of the exponential function would be absent, giving a somewhat faster decline towards high redshift. To understand how fast this suppression develops with redshift, we need to understand the scaling of $\sigma_4(z)$ and $q(z)$ separately.

3.3 The scaling of $\sigma_4(z)$

If we approximate the power spectrum on the scales of interest by a power law, $P(k) \propto k^n$, then the density fluctuations scale as $\sigma^2(M) \propto M^{-(n+3)/3}$ at fixed redshift. Based on equation (9), we hence have

$$\sigma_4^2(z) \propto D^2(z) [M_4(z)]^{-\frac{n+3}{3}} \propto D^2(z) [\chi(z)]^{\frac{n+3}{2}}, \quad (25)$$

where in the last step we made use of the conversion between mass and temperature defined in equation (14), and we used our definition of $\chi(z)$ given in equation (3).

Let us now consider the growth factor. Restricting ourselves to spatially flat cosmologies, we can write it as

$$D(z) = D_0 H_0^{-2} \Omega_0^{1/3} \chi^{3/2}(z) \int_{\chi(z)}^{\infty} \frac{dy}{y^{7/2}} \left(1 - \frac{\Omega_\Lambda}{y^3}\right)^{-\frac{1}{3}}. \quad (26)$$

Because we have $\Omega_\Lambda/y^3 < 1$, we can expand the integrand in a Taylor series and integrate term by term. This gives

$$D(z) = D_0 H_0^{-2} \Omega_0^{1/3} \chi^{-1} \left[1 + \frac{5}{33} \frac{\Omega_\Lambda}{\chi^3} + \mathcal{O}(\chi^{-6})\right]. \quad (27)$$

Therefore, to lowest order we have

$$D(z) \propto \frac{1}{\chi(z)}, \quad (28)$$

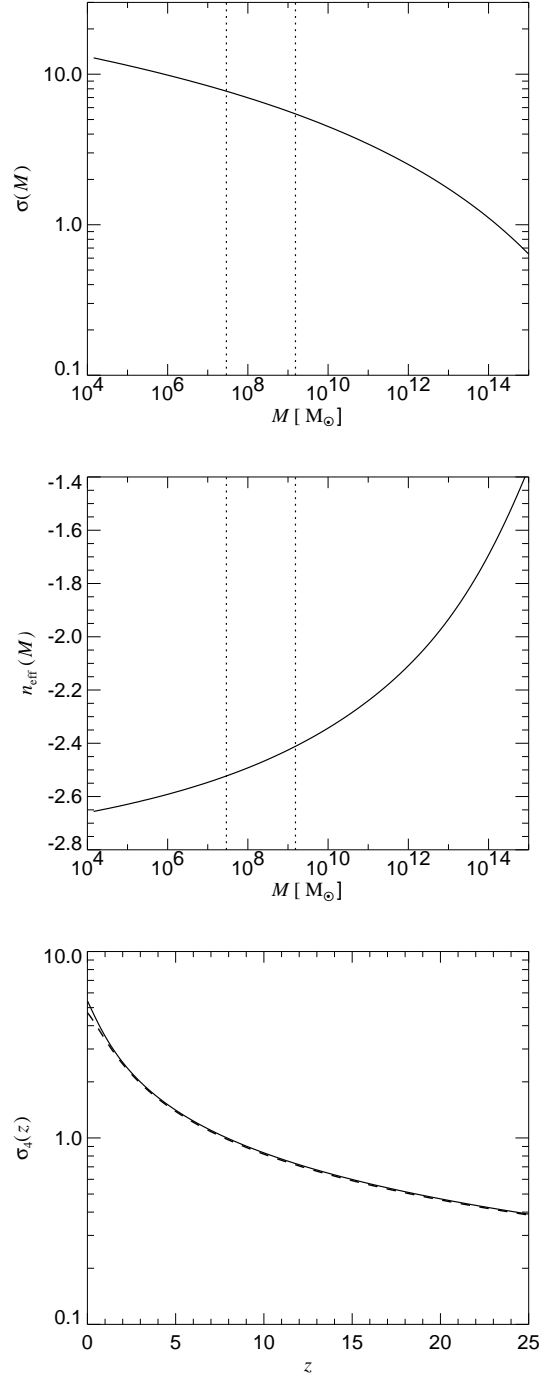


Figure 3. Top panel shows the rms-fluctuations $\sigma(M)$ in top-hat spheres that enclose a background mass M , for the present day linear power spectrum of a Λ CDM cosmology. In the middle panel, we show the corresponding effective slope of the power spectrum, defined here as $n_{\text{eff}} = -3 - 6 \text{dlog}\sigma/\text{dlog}M$. The dotted vertical lines indicate the range of masses that correspond to a virial temperature of 10^4 K between $z = 20$ (left line) and $z = 0$ (right line). In the bottom panel, we show the evolution of $\sigma_4(z)$ for the Λ CDM cosmology. The dashed line shows the approximation of equation (30).

which is accurate to better than 15% for the Λ CDM cosmology. Combining this with the result obtained in equation (25), we then arrive at the expected scaling of $\sigma_4(z)$ in the form of

$$\sigma_4(z) \propto \chi^{\frac{n-1}{4}}. \quad (29)$$

In Figure 3, we show the rms-fluctuations $\sigma(M)$ for the linear present-day power spectrum of a Λ CDM cosmology, together with its effective slope. On the mass scales that correspond to a virial temperature of 10^4 K, we find that n varies in the range -2.53 to -2.43 between $z = 20$ and $z = 0$, so that we can approximate it with $n \simeq -2.5$. In the bottom panel of Figure 3, we compare an exact computation of $\sigma_4(z)$ with our predicted scaling of

$$\sigma_4(z) = 4.7\chi^{\frac{n-1}{4}}, \quad (30)$$

using this effective slope of $n = -2.5$. The maximum error is $\simeq 13\%$ and occurs at the present epoch, where our approximation of the growth factor starts to lose precision, but this accuracy is still sufficient for our purposes.

3.4 The scaling of $q(z)$

Above, we have made the approximation that the evolution of the halo mass function depends only on gravitational physics, and as such can be described by the well-established results for non-linear structure formation in cold dark matter universes. It is clear, however, that the evolution of the star formation efficiency involves more complicated baryonic processes as well. Unfortunately, the relevant physics of radiative cooling, star formation, and feedback, is much less well understood.

In the simulations presented in Springel & Hernquist (2002b), we used a novel parameterisation of star formation and feedback in terms of a sub-resolution model of a two-phase interstellar medium (Springel & Hernquist, 2002a). In addition, we included strong galactic winds as a phenomenological extension of the model. Despite the complexity of these physical processes, we found that the normalised rate of star formation followed the simple factorisation suggested in equation (16); i.e. the shape of $s(M, z)$ remains approximately invariant when expressed as a function of virial temperature, while the amplitude of $s(M, z)$ scales with redshift.

Our results indicated that the normalised star formation rate scales steeply with redshift, roughly as $\sim (1+z)^3$, over the redshift range $2 < z < 7$. At redshifts below about $z \sim 2$, this evolution clearly appeared to slow down, however. At very high redshifts, for $z > 7$, the scaling also became much slower, apparently becoming approximately constant towards even higher redshifts.

We here argue that in the context of our model for star formation and feedback this behaviour can be understood in terms of two effects:

(i) At low and intermediate redshifts, cooling is relatively slow, such that one can ultimately expect that, at fixed virial temperature, the star formation rate scales in proportion to the cooling rate of a halo. For very massive halos, this is evident, because due to the inefficiency of feedback in massive halos, the supply of fresh cold gas directly governs the star formation rate. For smaller halos, feedback processes make star formation less efficient than the cooling rate, but

the resulting net amplitude can still be expected to vary in proportion to the cooling rate of the halo, provided that the dynamical equilibrium between star formation, cooling and feedback responds linearly to variations in the cooling rate.

(ii) At very high redshifts, cooling is rapid because of the high mean density of halos, but the strength of feedback processes in halos of fixed virial temperature remains unchanged. We should then encounter a regime where the star formation rate is no longer determined by the cooling rate, but instead by the gas consumption timescale t_0^* used in our multi-phase model of star formation (see Springel & Hernquist, 2002a). In this regime, we can picture the gas within halos to be cooling so rapidly that it essentially all becomes cold instantly, so that the star formation rate would asymptote to something of order $\sim M_{\text{cold}}/\langle t^* \rangle$, with M_{cold} being roughly equal to the total gas mass in the halo, and $\langle t^* \rangle$ being of order t_0^* (slightly smaller probably because of the decline of the consumption timescale towards higher density).

We now try to make this picture more quantitative. For the first point, we need an estimate of the cooling rate and how it scales with redshift. In order to obtain this, we use a variant of the cooling model employed in Springel et al. (2001) and Yoshida et al. (2002), which in itself is similar to the model of White & Frenk (1991).

The model starts by assuming that the hot gas is distributed according to a spherically symmetric profile $\rho_g(r)$ within a halo, with the gas being at the halo virial temperature T . We define a local cooling time by

$$t_{\text{cool}}(r) = \frac{3kT\rho_g(r)}{2\mu n_{\text{H}}^2(r)\Lambda(T)}, \quad (31)$$

where $n_{\text{H}}(r)$ is the number density of hydrogen, μ the molecular weight, and $\Lambda(T)$ the cooling function.

If the density profile is assumed to remain approximately fixed during cooling, the gas in the halo will have cooled at time t out to a radius $r_{\text{cool}}(t)$ given by

$$t_{\text{cool}}[r_{\text{cool}}(t)] = t. \quad (32)$$

This allows the cooling rate to be estimated as

$$\frac{dM_{\text{cool}}}{dt} = 4\pi\rho_g(r_{\text{cool}})r_{\text{cool}}^2\frac{dr_{\text{cool}}}{dt}. \quad (33)$$

Most of the cooling models used in semi-analytic calculations of galaxy formation are based on this equation, but they vary in the assumptions made about the profile $\rho_g(r)$, and the perhaps more uncertain question as to what time t should be used in equation (32). For example, White & Frenk (1991) have proposed using the age of the universe for t . It has also been argued that t should be the time elapsed since the last major merger of a halo (Somerville & Primack, 1999). Springel et al. (2001) suggest using the dynamical time of the halo instead, arguing that the gas profile should react to pressure losses from cooling on this timescale, and hence the cooling radius can on average be expected to grow to a radius corresponding to this time.

None of these choices can be rigorously justified without treating the dynamics of the gas self-consistently, which is beyond the scope of a simple analytic estimate. However, Yoshida et al. (2002) have directly compared cooling rates measured in hydrodynamic simulations with the above semi-analytic cooling model and find quite good agreement for a

parameterisation where the ansatz with the dynamical time was used. We will therefore choose it in what follows.

For the gas profile, a truncated isothermal sphere with $\rho(r) \propto r^{-2}$ is often adopted. To allow the possibility that the gas profile may have a different slope than an isothermal one at the typical cooling radius, we write the density profile in a slightly more general form as

$$\rho_g(r) = \frac{(3 - \eta) M_{\text{gas}}}{4\pi R_{\text{vir}}^{3-\eta} r^\eta}, \quad (34)$$

so that the profile behaves as $\rho(r) \propto r^{-\eta}$ at the typical cooling radius. From equation (32) we find

$$\frac{dr_{\text{cool}}}{dt} = \frac{1}{\eta} \frac{r_{\text{cool}}}{t_{\text{cool}}}. \quad (35)$$

Noting that we set $t_{\text{cool}} = t_{\text{dyn}} \equiv R_{\text{vir}}/V_{\text{vir}}$, we then obtain

$$r_{\text{cool}} = \left[\frac{(3 - \eta) M_{\text{gas}} R_{\text{vir}}^{\eta-2}}{4\pi f(T) V_{\text{vir}}} \right]^{\frac{1}{\eta}}, \quad (36)$$

where we defined the abbreviation

$$f(T) = t_{\text{cool}}(r) \rho_g(r) = \frac{3m_H^2 kT}{2\mu X^2 \Lambda(T)}, \quad (37)$$

and X is the hydrogen mass fraction. The cooling rate follows as

$$\frac{dM_{\text{cool}}}{dt} = \frac{3 - \eta}{\eta} f_b M_{\text{vir}} \left[\frac{(3 - \eta) f_b}{4\pi G f(T)} \right]^{\frac{3-\eta}{\eta}} [10H(z)]^{\frac{3}{\eta}}, \quad (38)$$

with $f_b \equiv M_{\text{gas}}/M_{\text{vir}}$.

We can now quantitatively check how well this estimate of the cooling rate explains the values of the star formation rate we measured in our simulations for large halos at late times. Recall that we argued that, for halos large enough to be unaffected by feedback effects, the star formation rate should essentially be given by the cooling rate. This should then clearly be the case for a virial temperature of 10^7 K, for example. This is because the galactic winds of our simulations, which leave star forming regions at a velocity of up to $v_{\text{wind}} = 484 \text{ km s}^{-1}$, can at most heat gas up to temperatures of $\sim 5 \times 10^6$ K when they are stopped, and they are expected to be unable to escape the gravitational potential well of halos with virial temperatures significantly larger than $\sim 10^6$ K.

In Figure 4, we show the measurements of $s(M, z)$ we made at a virial temperature of 10^7 K. We compare this data to the cooling rate predicted by equation (38), noting that the cooling function has a value of

$$\Lambda(T)/n_H^2 \simeq 10^{-23} \text{ erg cm}^3 \text{ s}^{-1} \quad (39)$$

at $T = 10^7$ K. We expect that we should find roughly $s \simeq \dot{M}_{\text{cool}}/M_{\text{vir}}$, and in fact, an almost perfect fit is obtained for $\eta = 1.65$ out to redshift $z \sim 7$. Given that the cooling model is rather crude, this level of agreement is remarkable. On the other hand, because the cooling model is so simple, one should probably take the good fit for $\eta = 1.65$ with a grain of salt, and grant that a different value in the range $\eta = 1.5 - 2$ may also be acceptable. Note, however, that $\eta = 1.65$ does quite a bit better in reproducing the shape traced out by the measurements than the isothermal value $\eta = 2.0$, which would predict a result lying a bit above the measurements. Also note that for $\eta \simeq 1.5$, the model predicts a scaling

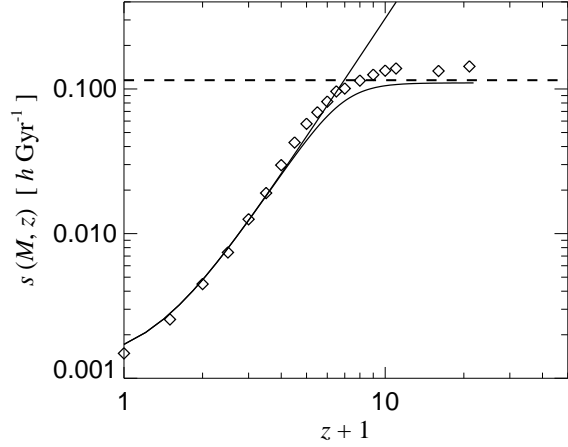


Figure 4. Comparison of the measurement of $s(M, z)$ from the simulations (symbols) at a fixed virial temperature of $T = 10^7$ K with estimates based in the cooling rate (solid), and on the “limit” argument (dashed).

$\propto H(z)^2$, which is essentially equal to the $\propto (1+z)^3$ scaling that we had guessed empirically at intermediate redshift.

However, at high redshift, the measurements for $s(M, z)$ clearly fall short of this scaling and instead appear to approach some kind of limit. This brings us back to the second point discussed above, where we argued that the model used to describe star formation implicitly imposes a maximum on the star formation rate in a given halo. If essentially all the gas in a halo has cooled, we expect of order $f_b M_{\text{vir}}$ of cold gas, where $f_b = \Omega_b/\Omega_0 = 0.133$ is the universal baryon mass fraction. In our model for star formation, a fraction $x \sim 0.95$ of this cold gas is in clouds, such that the maximum star formation rate can be estimated as $\dot{M}_* \sim (1 - \beta)x f_b M_{\text{vir}} / \langle t^* \rangle$, where $\beta = 0.1$ is the mass fraction of short-lived stars. The typical star formation timescale (t^*) of the gas will be somewhat smaller than the parameter t_0^* used in our star formation model, because of the density dependence of the consumption timescale. If we roughly estimate $\langle t^* \rangle = 2/3 t_0$, then we obtain $\dot{M}_*/M_{\text{vir}} \simeq 0.12 h \text{ Gyr}^{-1}$, in quite good agreement with the suggested maximum value based upon the measurements, as seen in Figure 4.

We can incorporate this maximum value into our expected scaling of

$$q(z) = \chi \frac{z}{2\eta} \quad (40)$$

based on the cooling rate alone, by making the replacement

$$\chi \rightarrow \frac{\chi \tilde{\chi}}{(\chi^m + \tilde{\chi}^m)^{\frac{1}{m}}}, \quad (41)$$

where $\tilde{\chi}$ is a constant that limits $\chi(z)$ at high redshift. This functional form provides a smooth transition between the regime that is governed by $q(z) = \chi \frac{z}{2\eta}$, and the one where $q(z)$ becomes constant. For larger values of m , the transition can be made sharper. We obtain a good match to our simulation results for $\tilde{\chi} = 4.6$ and $m = 6$, as shown in Figure 4.

In summary, the above discussion gives a plausible quantitative explanation for the behaviour of the normalised star formation rate in halos massive enough such that feed-

back effects are unimportant. However, for halos of small virial temperature, the simple derivation given above breaks down to some extent, because here feedback processes and winds *are clearly important*. In particular, the star formation rates measured for low mass halos in our simulations are substantially smaller than expected based on the cooling rate alone. At a fixed epoch, $\bar{s}(T)$ assumes a value about 3 times smaller for virial temperatures below $\sim 5 \times 10^6$ K than at the peak at $\simeq 10^7$ K. We argue that this behaviour is largely caused by feedback processes, notably by galactic winds. Nevertheless, the scaling of the star formation rate with redshift can still be described in terms of $q(z)$ given in equations (40) and (41).

3.5 A general fitting formula

Summarising the above, we have derived an analytic expression for the expected evolution of the star formation rate with redshift. Focusing on the Sheth & Tormen mass function in the following, which is known to provide a very good fit to the mass function measured in cosmological simulations, we have

$$\dot{\rho}_*(z) = \bar{\rho}_0 s_0 \left[\frac{\chi \tilde{\chi}}{(\chi^m + \tilde{\chi}^m)^{\frac{1}{m}}} \right]^{\frac{9}{2\eta}} \frac{1}{1 + \frac{5}{2} \sqrt{\pi} u \exp(u^2)}, \quad (42)$$

where $u = \sqrt{a/2} \delta_c / \sigma_4(z) \simeq 0.21 \chi^{7/8}$, and $\chi(z) = [H(z)/H_0]^{2/3}$. Recall that we determined $\tilde{\chi} = 4.6$, $\eta = 1.65$, and $m = 6$ as a fit to the scaling of the normalised star formation rate in halos of fixed virial temperature.

In Figure 5, we compare this equation to the direct simulation result. We see that the shape is indeed reproduced very well by the fitting function. The fit is nearly perfect, except that the ratio of high-redshift to low-redshift star formation appears not to be fully correct yet. When normalised to the star formation seen at high z , the analytic expression predicts slightly too little star formation at low redshift.

The reason for this lies in our very simplistic threshold model for the variation of the normalised star formation rate with temperature, which neglected the fact that the star formation efficiency is actually not strictly constant for temperatures above 10^4 K. Indeed, the presence of feedback by galactic winds maintains the normalised star formation rate roughly at a constant level for temperatures below $\simeq 10^{6.5}$ K, above which it rises to about three times higher.

We can incorporate this effect roughly into our model for the scaling of the normalised star formation rate by replacing equation (17) with

$$\tilde{s}(T) q(z) = \begin{cases} s_0 q(z) & \text{for } 10^4 \text{ K} < T < 10^{6.5} \text{ K}, \\ 3s_0 q(z) & \text{for } 10^{6.5} \text{ K} < T, \\ 0 & \text{otherwise.} \end{cases} \quad (43)$$

We can easily predict the star formation rate for this ansatz using the equations derived previously. All we need is the scaling of $\sigma_{6.5}(z)$, the rms-fluctuations in spheres of mass-scale corresponding to a virial temperature $10^{6.5}$ K. For this, we obtain

$$\sigma_{6.5}(z) \simeq 1.5 \chi^{\frac{n'-1}{4}}, \quad (44)$$

and note that the effective slope of the power spectrum on these mass scales is $n' \simeq -2.1$. This allows us to write the

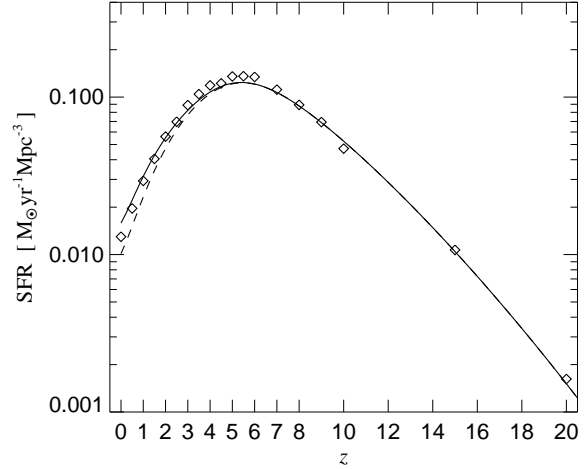


Figure 5. Comparison of simulation results for the cosmic star formation history (symbols) with expectations based on analytic estimates. The dashed line shows the result of equation (42), where all halos with higher virial temperature than 10^4 K were assumed to form stars with equal efficiency. The solid line shows the model of equation (45), where an additional contribution from halos more massive than $10^{6.5}$ K was included.

star formation history as

$$\dot{\rho}_*(z) = \bar{\rho}_0 s_0 \left[\frac{\chi \tilde{\chi}}{(\chi^m + \tilde{\chi}^m)^{\frac{1}{m}}} \right]^{\frac{9}{2\eta}} \left[\frac{1}{1 + \frac{5}{2} \sqrt{\pi} u \exp(u^2)} + \frac{2}{1 + \frac{5}{2} \sqrt{\pi} v \exp(v^2)} \right] \quad (45)$$

with v being defined as $v = \sqrt{a/2} \delta_c / \sigma_{6.5}(z) \simeq 0.67 \chi^{0.78}$, based on the scaling of $\sigma_{6.5}(z)$.

We also show this expression in Figure 5, where it is seen that it fits our simulation results very well. Also note that the normalisation for s_0 we picked here is only about $\sim 10\%$ different from the value predicted by Figure 4, if one identifies the $z = 0$ measurement of this 10^7 K halo with $3s_0$. We think that this good agreement is quite encouraging, showing that we have correctly modelled the effects that determine the evolution of the cosmic star formation density in our simulations.

It is interesting to consider the low and high redshift behaviour of the above expressions separately. At high redshift, the normalised star formation rate loses its redshift dependence, and only halos of virial temperature 10^4 K and slightly above contribute significantly to the star formation rate. Furthermore, we have $u \gg 1$ in this regime, so that the star formation rate then scales as

$$\dot{\rho}_*(z) \propto \chi^{\frac{n-1}{4}} \exp\left(-\beta \chi^{\frac{1-n}{2}}\right), \quad (46)$$

where

$$\beta = a \delta_c^2 / [2\sigma_4^2(0)] = 0.044, \quad (47)$$

and $n = -2.5$ is the appropriate effective slope of the power spectrum. It is important to note that this exponential decline of the star formation rate towards high redshift is directly related to the growth of the mass function, and has a

purely gravitational origin. It arises as a consequence of the threshold behaviour of the star formation rate, which is in itself caused by the properties of atomic line cooling. Despite this, the high-redshift behaviour of the star formation rate is generic, and independent of details of star formation itself. Interestingly, the decline towards high redshift depends on the shape and normalisation of the power spectrum.

Note that the decline of $\log \dot{\rho}_*$ towards high redshift is not strictly linear in redshift, as we had suspected earlier when deriving a first empirical fit to our simulation results. However, over the limited redshift range $6 < z < 20$, the scaling of equation (45) is well fit by a simple $\propto \exp(-z/3)$, which we had guessed originally. But at still higher redshift, we expect the star formation rate to decline significantly faster than this.

At low redshift, the normalised star formation rate scales as $q(z) \propto \chi^{\frac{9}{2\eta}}$, while the exponential growth of the mass fraction above the star formation threshold of 10^4 K essentially ends, being replaced by a comparatively slow residual increase. The combination of these two effects leads to the decline of the star formation density at low redshift.

To examine the low redshift behaviour itself, we note that equation (23) can be further simplified, because y lies in a limited range between 0.2 and 0.8 for $0 < z < 5$. We can then use the approximation

$$\frac{1}{1 + \frac{5}{2}\sqrt{\pi}y \exp(y^2)} \simeq \frac{1}{10y}, \quad (48)$$

which is good to better than 10% in the range $0.2 < y < 0.8$. Noting that $1/y \propto \sigma_4$, we therefore expect the low-redshift star formation rate to scale as

$$\dot{\rho}_*(z) \propto \chi^{\frac{9}{2\eta} + \frac{n-1}{4}}. \quad (49)$$

Since at very low redshift, the additional contribution of halos more massive than $10^{6.5}$ K begins to dominate, it may be more appropriate to use the effective slope of $n' = -2.1$ in this equation instead of $n = -2.5$ for the M_4 mass scales.

A simple analytic form that smoothly joins the low- z behaviour (49) and the high redshift scaling (46) is given by

$$\dot{\rho}_*(z) = \dot{\rho}_*(0) \frac{\chi^{\frac{9}{2\eta} + \frac{n'-1}{4}}}{1 + \alpha(\chi - 1)^{\frac{9}{2\eta} + \frac{n'-n}{4}} \exp\left(\beta \chi^{\frac{1-n}{2}}\right)}. \quad (50)$$

The exponent of χ in the numerator can be approximated as $9/(2\eta) + (n' - 1)/4 = 1.95 \simeq 2$. Similarly, the exponent of χ in the denominator is approximately $9/(2\eta) + (n' - n)/4 = 2.83 \simeq 3$, while the exponent in the argument of the exponential function is $(1 - n)/2 = 7/4$. We can hence consider a simplified fitting function of the form

$$\dot{\rho}_*(z) = \dot{\rho}_*(0) \frac{\chi^2}{1 + \alpha(\chi - 1)^3 \exp(\beta \chi^{7/4})}. \quad (51)$$

This is the expression we proposed at the onset of our analysis. Compared to our full analytic estimate of the evolutionary history, it has the advantage of a simpler analytic form, but involves a fitting parameter α . For $\alpha = 0.012$ and $\beta = 0.041$, we obtain a very good fit to our simulation result, as seen in Figure 1. Note that β is in principle determined by equation (47), and thus depends directly on the normalisation of the power spectrum. The reason why we here lowered β slightly from 0.044 to 0.041 was just to approximately

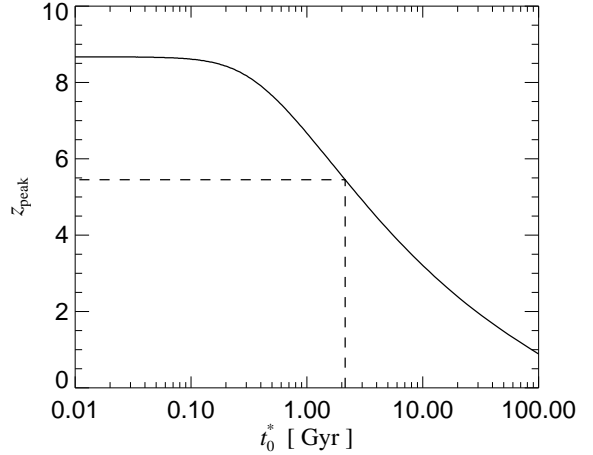


Figure 6. The redshift position of the peak of the cosmic star formation history as a function of the star formation timescale t_0^* used in our multi-phase model. For our adopted normalisation, which matches the observed star formation rates in present-day spiral galaxies, the peak occurs at redshift $z_{\text{peak}} = 5.45$. However, even if an arbitrarily short gas consumption timescale is chosen, the peak cannot be pushed to higher redshift than $z_{\text{peak}} \simeq 8.7$.

compensate the increase of the leading exponent of χ in the denominator from 2.83 to 3 that we made.

3.6 The peak of the star formation history

As we have seen, with time the star formation rate falls at low redshift, while it increases at high redshift. In between, a peak must obviously occur. It is interesting to examine what determines the location of this peak in our model.

At moderately high redshift, it is sufficient to consider equation (42) as the prediction of our star formation model, because then the extra contribution of star formation from halos more massive than $10^{6.5}$ K can be neglected. Interestingly, the location of the maximum of this curve is independent of s_0 , but is somewhat sensitive to the prescribed maximum of the normalised star formation rate in our model, as imposed by the value of $\tilde{\chi}$. If we assume that such a maximum does not exist, i.e. for $\tilde{\chi} \rightarrow \infty$, then the star formation rate peaks at a redshift $z_{\text{peak}} = 8.67$, independent on the details of our modeling of star formation. For any finite value of $\tilde{\chi}$, the peak of the star formation history will occur at a lower redshift.

This highlights that the exponential decline of the abundance of star-forming halos at high redshift will always overwhelm any power-law scaling of the star formation efficiency with expansion rate, even if this scaling is very steep, as assumed here. Consequently, it is not possible to push the peak of the star formation history to arbitrarily high redshift. In particular, if the cooling rate is indeed limiting the star formation rate in the way found here, the peak must occur below a redshift of $z \simeq 8.7$ in the Λ CDM cosmology.

We obtain further insight about the dependence of the peak's position on model parameters by recalling that we were able to relate the maximum normalised star formation rate to the gas consumption timescale t_0^* , where t_0^* is the free

parameter of our hybrid multi-phase model for star formation (Springel & Hernquist, 2002a). In particular, we expect that $\tilde{\chi}$ will vary as $\tilde{\chi}^{\frac{9}{27}} \propto 1/t_0^*$ when the model parameter t_0^* is varied. For the simulations analysed here, t_0^* was set to $t_0^* = 2.1$ Gyr by normalising the star formation rate of disk galaxies to the empirical Kennicutt Law (Kennicutt, 1989, 1998) at $z = 0$.

In Figure 6, we show the expected location of the peak of the star formation history when t_0^* is modified with respect to our fiducial choice of 2.1 Gyr, with its corresponding peak at $z_{\text{peak}} = 5.45$. To delay the peak to a redshift as low as $z = 3$, the gas consumption timescale would have to be increased by about a factor of 5 to an uncomfortably high value of $\simeq 10$ Gyr. Note in particular that this would make us miss the normalisation of the Kennicutt Law by about the same factor, and would spoil our match of the observed density threshold for the onset of star formation in disk galaxies.

4 DERIVED QUANTITIES

The cosmic star formation history directly determines a wide range of key observables of the universe. Making use of the computational simplification provided by the analytic fit for the star formation density derived above, we can conveniently obtain a number of such predictions. Clearly, this application is one of the main reasons why an analytic closed-form description of the star formation history is valuable. Among the range of direct implications of the star formation history, we will here consider the stellar density and metal enrichment history of the universe, the observable supernova and GRB rates on Earth, and the expected evolution of the density of compact objects.

4.1 Stellar density

The mass density of long-lived stars that have formed at redshifts higher than z is simply given by

$$\rho_*(z) = \int_0^{t(z)} \dot{\rho}_* dt = \int_{\chi(z)}^{\infty} \dot{\rho}_*(\chi) \frac{\chi^{1/2}}{H_0(\chi^3 - \Omega_\Lambda)} d\chi. \quad (52)$$

Note that for the last equality we assumed a flat cosmology. If we express the stellar density in units of the baryon density, we obtain the fraction

$$f_*(z) = \frac{\rho_*(z)}{\rho_b} \quad (53)$$

of baryons locked up in stars at a certain redshift, where $\rho_b = \Omega_b \rho_{\text{crit}}$. Using our fitting function (2) and the cosmological parameters of our simulations ($\Omega_b = 0.04$, $\Omega_\Lambda = 0.7$), we obtain $f_*(0) = 9.2\%$, in good agreement with our direct simulation result of 9.3%, and consistent with observational constraints (Cole et al., 2001; Balogh et al., 2001; Fukugita et al., 1998) once the baryons in the warm-hot IGM (Cen & Ostriker, 1999; Davé et al., 1999, 2001) are taken in account (Springel & Hernquist, 2002b). In Table 1, we give the redshifts and lookback times for which the cumulative number of stars has reached a certain fraction of the present day value. These numbers are also in good agreement with the corresponding simulation values given in Springel & Hernquist (2002b), confirming once more that the analytic fitting function accurately describes our simulation results.

Fraction	z	T [Gyr]
0.1	6.10	12.57
0.2	4.65	12.20
0.3	3.67	11.79
0.4	2.90	11.28
0.5	2.24	10.58
0.6	1.65	9.61
0.7	1.14	8.23
0.8	0.69	6.26
0.9	0.31	3.53

Table 1. Cumulative star formation history as a function of lookback time T and redshift z . In each row, we list the times at which a certain fraction $f_*(z)/f_*(0)$ of stars has formed.

4.2 Metal enrichment

Here, we make a rough estimate of the metallicity evolution of the universe, assuming instantaneous recycling. For every mass element dM_* of long-lived stars formed, a gas mass equal to $dM_Z = y dM_*$ is transformed to heavy elements and returned to the interstellar or intergalactic medium. Here y is the yield, which we assume to be independent of environment and epoch.

The metals deposited in the gas can either remain there, or they can become permanently locked up in long-lived stars forming out of enriched gas. If we define \bar{Z}_* as the mean mass-weighted metallicity of all stars, and \bar{Z}_{gas} as the mean metallicity of *all* remaining gas, then all metals produced up to a given epoch can be found either in stars or in the gas. This metal budget can thus be written as $y \rho_* = \bar{Z}_* \rho_* + (\rho_b - \rho_*) \bar{Z}_{\text{gas}}$, so that the mean mass-weighted metallicity of the gas follows as

$$\bar{Z}_{\text{gas}}(z) = \frac{\rho_*(z)}{\rho_b - \rho_*(z)} [y - \bar{Z}_*(z)] = \frac{y - \bar{Z}_*(z)}{f_*^{-1}(z) - 1}. \quad (54)$$

If there is no loss of metal-enriched gas from star-forming regions at all, we would expect that the mean metallicity of the stars should be almost equal to the yield y , the asymptotic value for a “closed-box” model. However, in our simulations, star-forming galaxies are “leaky”, and particularly at low mass scales, they can lose metals efficiently by galactic outflows. Observationally, there is also substantial evidence that metals are able to escape from star-forming regions, as for example shown by metal-absorption lines discovered in the low-density intergalactic medium. As a result, we expect $\bar{Z}_*(z)$ to be – perhaps considerably – smaller than y .

An accurate quantitative estimate of $\bar{Z}_*(z)$ requires a detailed modelling of the gas enrichment and transport processes occurring during galaxy formation, which is beyond the scope of this work. However, we can make a simple estimate for the amount of metals that can escape from small galaxies by winds. In the model that we used in our simulation work, winds are generated with a fixed velocity, and with a mass-loss rate equal to twice the star formation rate. An escaping wind can hence be expected to transport about 2/3 of the metals produced by the stars from the highly overdense interstellar medium into the intergalactic medium (IGM). The remaining 1/3 will be locked up in long-lived stars. Whether or not a wind can leave a star-forming galaxy depends to a large extent on the escape velocity of its halo,

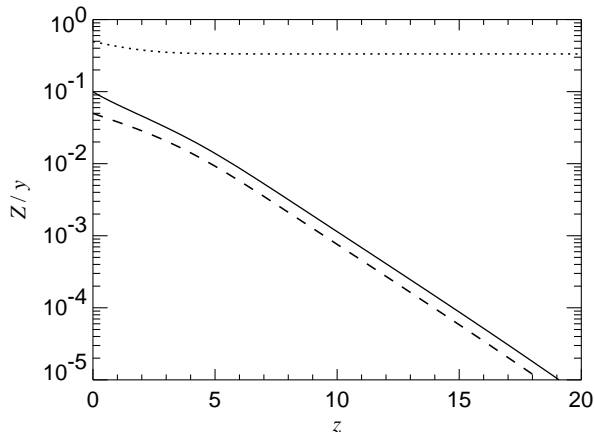


Figure 7. Upper limit for the mean mass-weighted metallicity of ambient gas as function of redshift, normalised to the assumed stellar yield y (solid line). The true mean metallicity will be lower by the amount of metals locked up in stars forming from enriched gas. Using a simple wind-escape model, we have also computed estimates for the mean metallicities of stars (dotted) and gas (dashed) when the leakage of metals from small galaxies by galactic winds is taken into account.

which in itself depends directly on its virial temperature. For simplicity, we here assume that winds can always escape from halos with virial temperature below $10^{6.5}$ K, while they stay completely confined in larger halos. These large galaxies then act much like closed-boxes, with most of the metals released by supernova ending up in long-lived stars. In this simple picture, we can then estimate the amount of metals in stars as

$$\bar{Z}_*(z)\rho_*(z) \simeq \frac{1}{3}y\rho'_*(z) + y[\rho_*(z) - \rho'_*(z)], \quad (55)$$

where ρ'_* describes the density of stars that have formed in halos of virial temperature below $10^{6.5}$ K. In this simple estimate, we neglected the possibility of “metal reaccretion” from the enriched IGM. Note that the rate ρ'_* at which stars form in halos smaller than $10^{6.5}$ K can be obtained by means of equation (45) if we replace the number 2 in the numerator of its last term by minus 1. The estimated mean metallicity of the gas then follows as $\bar{Z}_{\text{gas}} = 2y\rho_*/[(f_*^{-1} - 1)\rho'_*]$.

Clearly, a detailed analysis of hydrodynamical simulations will be required to check the accuracy of the above crude estimate. However, we note that neglecting $\bar{Z}_*(z)$ in equation (54) provides a strong upper limit for the mean gas metallicity as a function of epoch.

In Figure 7, we show the resulting upper limit $\bar{Z}_{\text{gas}}^{\text{max}}(z) = y/[f_*^{-1}(z) - 1]$ as a function of redshift, together with our estimates for the expected mean metallicities of stars and gas in the framework of the above wind-escape model. For a solar yield of $y \simeq 0.02$, the mean mass-weighted metallicity at $z = 3$ could hence reach values of up to 3.5×10^{-2} solar. However, since large galaxies are expected to confine most of the metals they produce, locking them up in long-lived stars, a more realistic estimate is the value of $\sim 2.0 \times 10^{-2}$ solar derived for the wind-escape model. Note, however, that we expect strong spatial variations in the metallicity of the gas, with a tendency of higher density

regions to be more metal rich. The actually observed metallicity of gas of mean cosmic density could hence be quite a bit lower than the above limits.

4.3 Supernova and GRB rate

For definiteness, we here assume a universal initial mass function (IMF) of Salpeter (1955) form with slope -1.35 in the mass range $0.1 M_\odot$ to $40 M_\odot$. We further assume that all massive stars above $8 M_\odot$ explode as supernovae after a short lifetime of $T_{\text{sn}} = 3 \times 10^7$ yr. The number of supernovae per unit mass of long-lived stars is thus given by

$$f_{\text{sn}} = \frac{\int_{8 M_\odot}^{40 M_\odot} f(M)M^{-1} dM}{\int_{0.1 M_\odot}^{8 M_\odot} f(M) dM} \simeq 7.9 \times 10^{-3} M_\odot^{-1}, \quad (56)$$

where $f(M) \propto M^{-1.35}$. Note that the star formation rate $\dot{\rho}_*(z)$ we considered in our simulations and in the analysis of this paper up to this point, is to be understood as the rate at which long-lived stars form. This rate does not include the formation rate of massive stars, which are instead assumed to explode instantaneously and to return all of their mass to the ambient gas.

The comoving number density of supernova explosions, \dot{n}_{sn} , is then simply expected to follow the star formation rate, retarded by the lifetime of massive stars:

$$\dot{n}_{\text{sn}}(t) = f_{\text{sn}} \dot{\rho}_*(t - T_{\text{sn}}). \quad (57)$$

The retardation effect can usually be neglected at low redshift, where the evolutionary timescale of the star formation rate is large compared to T_{sn} .

We may also ask at which rate supernova events could be detected by an observer on Earth, and what the redshift distribution of these events would be. Defining the comoving distance to an event at an observed redshift z as

$$d(z) = \int_0^z \frac{c dz'}{H(z')}, \quad (58)$$

the predicted rate of supernovae per unit redshift element and unit solid angle is given by

$$\frac{d\dot{N}_{\text{sn}}}{dz d\Omega}(z) = f_{\text{sn}} \dot{\rho}_*(z') \frac{c d^2(z)}{(1+z)H(z)}. \quad (59)$$

Here z' denotes the “retarded redshift” obtained by transforming z to lookback time, adding the supernova lifetime T_{sn} and transforming back to redshift. The factor $(1+z)$ in the denominator takes care of the cosmological time dilation effect.

In Figure 8, we show the redshift distribution of this observable supernova rate. Interestingly, the cosmological effects make the distribution peak at substantially lower redshift than the star formation rate density itself. Over the full redshift range, a total supernova rate of $d\dot{N}_{\text{sn}}/d\Omega = 1.27 \text{ s}^{-1} \text{ str}^{-1}$ is predicted, or about 15.9 per second over the whole sky. Unfortunately, most of these events will be too distant and hence too faint to ever be observable.

Of course, the total energy flux received from supernovae is much more peaked towards lower redshift than the event distribution itself. If, for simplicity, a supernova is modelled as a standard candle with a total bolometric emission of energy E in radiation, then the redshift distribution

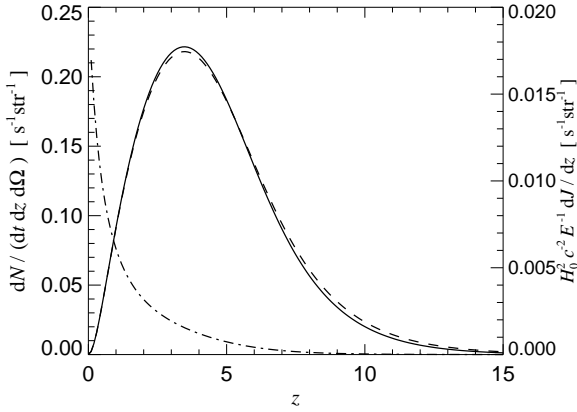


Figure 8. Distribution of the supernova rate per unit redshift interval as – in principle – observable on Earth (solid line). The dashed line shows our prediction if the time delay T_{sn} between formation and explosion of massive stars is neglected. The dot-dashed line gives the redshift distribution of the total specific intensity generated by the background of all supernovae.

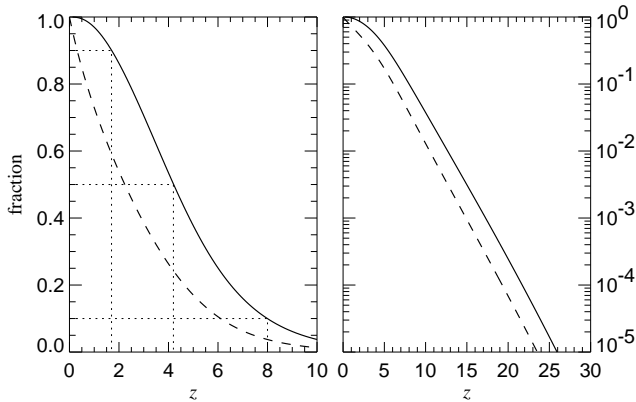


Figure 9. Fraction of all observable GRBs/supernovae that occur at redshifts higher than z (solid lines). The left and right panel differ only in the scaling of the y-axis. Also shown is the fraction $f_{\star}(z)/f_{\star}(0)$ of stars that have formed prior to a given redshift.

of the specific intensity of the total supernova background radiation is given by

$$\frac{dJ}{dz}(z) = \frac{c}{4\pi} E \frac{f_{\text{sn}} \dot{\rho}_{\star}(z')}{(1+z)^2 H(z)}. \quad (60)$$

In Figure 8, we have included a graph that shows the redshift distribution of this flux. About half the total energy received on Earth from supernovae originated at redshifts lower than $z = 1.3$, but these events are only 5.5% by number of all supernova events that are in principle arriving on Earth.

There could also be a close relation between the supernova rate and the rate of gamma ray bursts (GRBs) observed on Earth. While the origin of GRBs is still one of the most interesting *open* questions in cosmology, there are now a number of promising theoretical models that link them to compact objects (black holes or neutron stars) that form as end products of the evolution of very massive stars. This

suggests that the rate of GRBs should directly follow the star formation rate, just like the supernova rate that we considered above. Consequently, the observable GRB rate can be computed in the same way as the supernova rate, with f_{sn} being replaced by the expected (but uncertain) number f_{grb} of GRBs per unit-mass of long-lived stars. Bromm & Loeb (2002) have recently given a detailed analysis of the expected GRB rate based on an estimate along these lines.

In Figure 9, we show the fraction of all observable GRBs that originated at redshift higher than a given epoch. Note that the corresponding fraction of supernovae is identical if the time delay T_{sn} is neglected. For comparison, we also give the integrated fraction $f_{\star}(z)/f_{\star}(0)$ of stars that have formed up to a given redshift. Clearly, the distribution of observable GRBs/supernovae is biased towards higher redshift compared to the redshift distribution of all stars, even though the GRB/supernova rate peaks actually at lower redshift than the star formation history itself. About 50% of the observable supernovae/GRBs are expected to originate beyond redshift $z \simeq 4.2$, while it takes until redshift 2.2 before 50% of all stars are formed. Bromm & Loeb (2002) have assumed a different star formation history with a larger star formation rate at high redshift. Consequently, they estimated a slightly higher redshift of about $z \simeq 5$ for the epoch at which 50% of the GRB signals have been generated. Note however that the GRB rate could be quite sensitive to variations of the IMF with redshift, and to the possible existence of high-redshift star formation mediated by molecular cooling, which we neglected here.

4.4 Density in compact objects

So far, we have assumed that stars below a mass of $8 M_{\odot}$ live essentially forever. However, especially the more massive ones among them should have reached the end of their lifetime by the present day, provided they have formed early enough in the history of the universe. Depending on their mass, they can then become transformed into compact objects like white dwarfs or neutron stars, for example.

We here want to compute a rough estimate for the fraction of stars that have died since their formation time, but without going into the complexities of full stellar evolution theory. We therefore crudely assume that a star of mass M has a lifetime of order

$$T_{\star}(M) \simeq T_{\odot} \left(\frac{M}{M_{\odot}} \right)^{-2.3}, \quad (61)$$

where we put $T_{\odot} = 10$ Gyr as the approximate lifetime of a solar mass star. Neglecting any mass-loss processes during the final stages of stellar evolution, the formation rate of “compact objects” is then given by

$$\dot{\rho}_{\text{c}}(t) = \int_{0.1 M_{\odot}}^{8 M_{\odot}} dM f(M) \dot{\rho}_{\star}[t - T_{\star}(M)], \quad (62)$$

where $f(M)$ describes the normalised Salpeter IMF. This quantity may also be viewed as an estimate of the death rate of ordinary stars.

In Figure 10, we show the history of the mass-weighted formation rate of compact objects. As expected, the death rate of stars peaks at lower redshift than the star formation rate itself, which is simply a result of the dilation effect

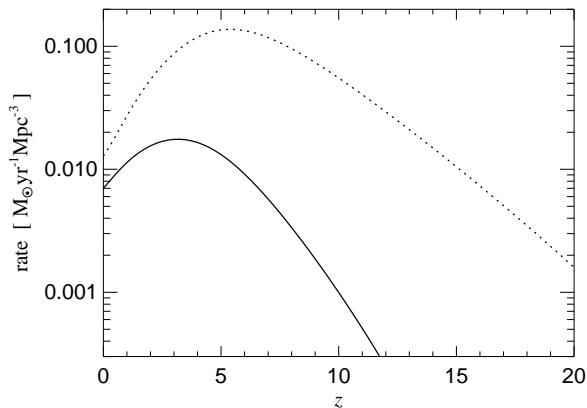


Figure 10. Formation rate $\dot{\rho}_c$ of compact objects as a function of redshift (solid line). For comparison, we also show the formation rate of long-lived stars (dotted line).

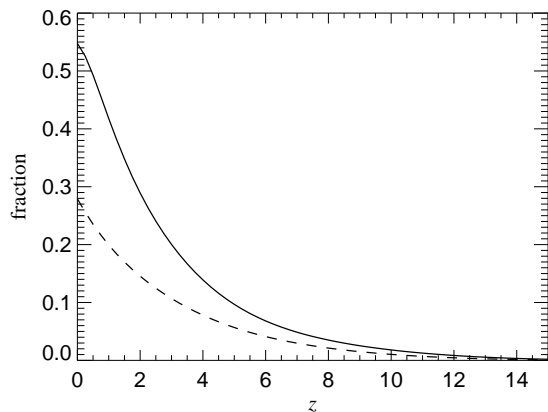


Figure 11. The ratio $\dot{\rho}_c/\dot{\rho}_*$ of the rate of stellar deaths to the star formation density (solid). At the present epoch, stars are already dying with more than half the rate at which new stars are being formed. The dashed line gives the mass fraction of long-lived stars that have turned into compact objects (i.e. that have reached the end of their stellar lifetimes) as a function of redshift.

due to the lifetime of stars. Note, however, that the mass-weighted rate of stellar deaths is already strongly declining at present, which is a non-trivial consequence of stellar lifetimes in relation to the cosmic star formation history. It is also interesting to compare the stellar death rate to the star formation rate directly. In Figure 11, we show the ratio $\dot{\rho}_c/\dot{\rho}_*$ of the two as a function of redshift. Interestingly, at the present epoch the rate of formation of compact objects has reached about half of the rate at which new stars are being formed, and $\dot{\rho}_c$ is set to exceed $\dot{\rho}_*$ in the not too distant future. In Figure 11, we also show the ratio of the cumulative density of stellar remnants to the density of stars. At $z = 0$, more than 25% of all formed stellar mass is expected to be in stars that have already reached the end of their ordinary stellar lifetimes.

5 DEPENDENCE ON MODEL PARAMETERS

5.1 Effects of cosmological parameters

The analysis of the physical origin of the cosmic star formation rate carried out in Section 3 allows us to investigate expected variations in its evolution as a function of cosmological parameters. To this end, it is perhaps easiest to consider equation (45), and to discuss the cosmological dependence of the various terms involved.

The scaling of the background density $\bar{\rho}_0$ is simply given by its definition; viz. $\bar{\rho}_0 = 3\Omega_0 H_0^2 / (8\pi G)$. Also, the dependence of $\chi(z)$ on cosmological parameters is straightforward and follows from the usual scaling of the Hubble constant. For the normalised star formation rate $s_0 \sim \langle M_* \rangle / M_{\text{vir}}$, we expect it to scale like the cooling rate normalised to the halo mass. Based on equation (38), this implies

$$s_0 \propto (f_b H_0)^{\frac{3}{7}}, \quad (63)$$

where $f_b = \Omega_b / \Omega_0$. A slightly more subtle question is how the parameter $\tilde{\chi}$, which limits the star formation efficiency, depends on cosmological parameters. Recall that the maximum star formation rate we expect in a halo of mass M_{vir} is given by $\simeq f_b M_{\text{vir}} / t_0^*$ in the multi-phase model considered here. On the other hand, we assumed that this maximum is just attained as $s_0 \tilde{\chi}^{\frac{9}{27}}$. If t_0^* depends only on “local physics” of the star forming gas, it should be approximately independent of cosmological parameters. We thus expect $\tilde{\chi}$ to scale as

$$\tilde{\chi} = 4.6 \left(\frac{\Omega_b / \Omega_0}{0.133} \right)^{-0.3} \left(\frac{h}{0.7} \right)^{-2/3}. \quad (64)$$

Finally, the shape and normalisation of the power spectrum influence the evolution and amplitude of $\sigma_4(z)$ and $\sigma_{6.5}(z)$, respectively. In particular, the high redshift behaviour of the star formation rate will be quite sensitive to the amplitude of $\sigma_4(z)$. The lower the amplitude, the larger the slope parameter β , implying a faster decline of the star formation rate towards high redshift.

In Figure 12, we show a few examples of star formation histories expected for different cosmological parameters. For simplicity, we mainly restrict ourselves to simple variants of the Λ CDM model. In particular, we show results for variations of the power spectrum normalisation in the top panel, and for changes of the baryonic density in the lower panel. It is clearly seen that the high redshift star formation rate is particularly sensitive to the normalisation of the power spectrum. This is also one of the reasons why a τ CDM model with critical density, which we show in the lower panel of Figure 12, is expected to feature a quite different star formation history with much less high-redshift star formation, and a peak at substantially lower redshift. The effects of the low normalisation of $\sigma_8 = 0.6$ of this model are further amplified by the different evolution of the growth factor as compared to the Λ CDM cosmology.

5.2 Effects of metal line cooling

It is well known that the cooling rate of gas can be increased substantially even by relatively little enrichment with heavy elements. This is particularly true in the temperature range $\sim 10^{4.5} - 10^{6.5}$ K, where an enrichment to solar metallicity

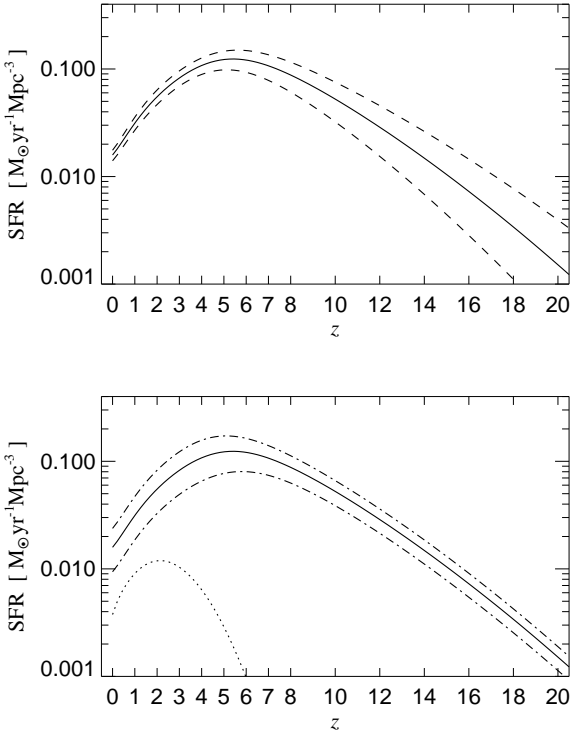


Figure 12. Examples of the expected dependence of the cosmic star formation history on cosmological parameters. In the top panel, we show the star formation density for the Λ CDM model when the normalisation of the power spectrum is changed to $\sigma_8 = 1.0$ or $\sigma_8 = 0.8$, respectively (upper and lower dashed lines). Similarly, the lower panel shows the effect when the baryon density is varied to $\Omega_b = 0.05$ or $\Omega_b = 0.03$, respectively (dot-dashed lines). In both cases, the solid lines give our standard result for the Λ CDM model, for comparison. Finally, the dotted line shows the result for a τ CDM model of critical density, with baryon density $\Omega_b = 0.08$, Hubble constant $h = 0.5$, and normalisation $\sigma_8 = 0.6$.

can increase the cooling rate by an order of magnitude, while even a low metallicity of $10^{-2} Z_\odot$ still enhances cooling by roughly a factor of two. At higher temperatures, the sensitivity to metal enrichment is significantly weaker, though.

So far, we have neglected the effect of metal enrichment on the cooling efficiency of gas, both in our simulations and in our present analysis. This might result in a systematic underestimate of the cooling and star formation rates, particularly at low redshift, where the average metallicity of gas reaches potentially important levels. However, whether the predictions we obtained in the framework of our model are really altered by metal enrichment in a significant way is less clear than it may seem, as we now discuss.

We first note that there are really two quite different regimes where the cooling rate of gas is important. There is on one hand the diffuse gas in galactic halos, which must dissipate its thermal energy radiatively in order to collapse onto the highly overdense interstellar medium (ISM) in the centres of galaxies. This is the principal supply channel for gas that becomes newly available for star formation.

On the other hand, there is the gaseous multiphase

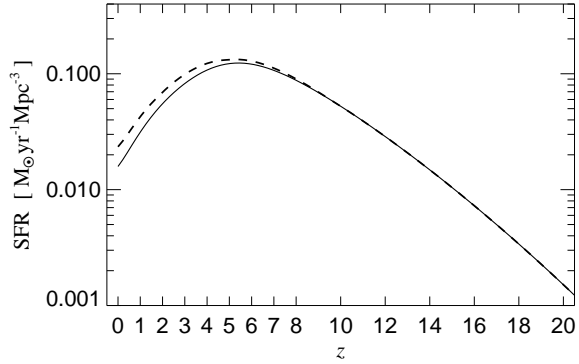


Figure 13. Estimate of the possible effect of metal line cooling on the cosmic star formation history. The dashed line represents our prediction when the metallicity dependence of the cooling function at $10^{6.5}$ K is taken into account, assuming a uniform metallicity following the predicted evolution of the mass-weighted mean metallicity of the gas. The solid line represents our default result of equation (45), for comparison.

structure within the ISM itself, where most of the baryonic mass is in cold clouds, but a small fraction of it fills the volume as a hot intercloud medium, heated by supernova explosions. This hot phase of the ISM is expected to reach high metallicity quickly as soon as local star formation starts, and it is hence in principal subject to very strong cooling enhancement by metal lines. However, within the simple model that we developed to describe the ISM, this metallicity effect can be offset by a slight adjustment of the adopted temperature structure of the ISM (as controlled by the evaporation efficiency A_0 , see Springel & Hernquist, 2002a), and to a lesser extent, by a small change of the gas consumption timescale, t_0^* . The parameters can be chosen such that the normalisation of the Kennicutt Law is maintained, yielding, to first order, an unaltered dynamical behaviour of the ISM model. While it hence may have been more consistent to assume high metallicity for the ISM to begin with, this would not have changed our model predictions but only the parameter values required to match the Kennicutt Law that we used as a normalisation constraint.

We are thus primarily left with the influence of metal enrichment on the cooling of gas within the diffuse atmospheres of halos. At high redshift, cooling is so efficient that we expect gas to cool nearly instantly, even without any enrichment with metals. In this regime, the evolution of the star formation rate is driven by the fast gravitational growth of the halo mass function, and we thus expect our results to be largely independent of metal enrichment.

However, at low redshift, cooling becomes inefficient and the supply of star forming gas is regulated by the cooling rate. Consequently, we expect that the star formation rates would be higher if the cooling gas is significantly enriched with heavy elements. Unfortunately, it is far from clear how efficiently metals that are expelled from the star forming ISM of galaxies are mixed with the rest of the gas in the universe. While small galaxies can efficiently expel metals with galactic winds into the IGM, where they are stopped by shocks, the resulting bubbles of metal-enriched

gas may be too hot to be accreted again by similarly small galaxies. Gas that cools onto these small galaxies may then always end up being mostly pristine. On the other hand, the metals deposited in the IGM may be “recollected” in the collapse of significantly larger objects, for example in galaxy groups or clusters, resulting in pre-enriched halos. In general, we expect larger halos to have a better chance of accreting metal-enriched gas. Note, however, that the relative enhancement of the cooling rate by metals becomes weaker for larger halos due to their higher virial temperatures.

Perhaps the simplest model we can make for estimating the possible influence of metal-line cooling on our prediction for cosmic star formation is to assume that the diffuse gas cools with the average gas metallicity that we estimated in section 4.2. For simplicity, we neglect the temperature dependence of the cooling enhancement at a given metallicity, and instead approximate it with the values appropriate for halos of virial temperature $\sim 10^{6.5}$ K. Halos with this temperature or higher dominate the star formation rate at low redshift. For halos larger than $10^{6.5}$ K, we will then overestimate the cooling enhancement effect, but this is offset to some extent by a possible underestimate for smaller halos, where the dependence of the cooling rate on metallicity is stronger.

In Figure 13, we show the resulting estimate for the evolution of the star formation rate when the enrichment history is taken into account by a global increase of the value of the cooling function for all halos, assuming a yield of $y = 0.02$. Note that we found earlier that the cooling rate scales slightly weaker than linear with the cooling function, as $\propto [\Lambda(T, Z)]^{(3-\eta)/\eta}$, which alleviates the metallicity dependence slightly. Nevertheless, we obtain an estimated increase of the star formation density of about 50% at $z = 0$. Because this metallicity effect becomes weaker towards higher redshift, the increase in the total stellar density is only about 25%.

Hence, metals have the potential to alter the star formation history at low redshift. However, more reliable estimates of the strength of this effect require a better understanding of the mixing processes of ejected metals with the gas. Depending on the details of these processes, the effects of metal enrichment may be more or less substantial than estimated here. Note that the importance of metal enrichment effects is also intimately linked to the strength of galactic winds, or more generally, to the physical nature of feedback processes. We remark that without the inclusion of winds, accreted gas from the IGM would always be pristine in our simulations.

6 DISCUSSION

We have formulated an analytical model to identify physical processes that play an important role in determining the evolution of the cosmic star formation rate density, $\dot{\rho}_*(z)$. Using this model, we obtain simple closed-form expressions for $\dot{\rho}_*(z)$ which match hydrodynamic simulations that include star formation and feedback to a level of $\approx 10\%$. Our model, therefore, provides a framework for interpreting both theoretical and observational estimates of $\dot{\rho}_*(z)$.

Our analysis shows that the evolution of the cosmic star formation rate is characterised by a number of generic features in hierarchical universes. These properties depend

on cosmological parameters but are largely insensitive to the detailed physics of star formation.

In particular, we have identified two broad regimes of star formation that are separated by a peak in $\dot{\rho}_*(z)$ at $z = z_{\text{peak}}$. At high redshifts, $z > z_{\text{peak}}$, cooling is very efficient and halos contain abundant quantities of star-forming gas. In this regime, the dominant contribution to the global star formation rate comes from the highest mass halos present at any time that are not unusually rare. Consequently, $\dot{\rho}_*(z)$ follows the evolution of the exponential part of the halo mass function. The logarithmic slope of this phase of evolution depends on properties of the cosmology but not on the details of star formation, which only affect the overall normalisation.

At low redshifts, $z < z_{\text{peak}}$, cooling becomes inefficient, and the supply of star-forming gas is regulated by the cooling rate. In this regime, $\dot{\rho}_*(z)$ gradually declines from its maximum at $z = z_{\text{peak}}$ to $z = 0$ as a power-law function of the expansion rate, $\dot{\rho}_*(z) \propto H(z)^q$. Typically, we find $q \approx 4/3$, weakly dependent on the gas density profiles within dark matter halos. The scaling may also be altered slightly if metal enrichment becomes important in halos at late times. To the extent that our results apply to the real Universe, observations of $\dot{\rho}_*(z)$ at $z < z_{\text{peak}}$ should be well-fitted by a functional form $\dot{\rho}_*(z) \propto H(z)^q$. Thus, our prediction for the evolution of the cosmic star formation rate is, in principle, testable by accurate measurements of $\dot{\rho}_*(z)$ at low redshifts.

We have shown that the existence of a peak in the star formation rate at a redshift $z = z_{\text{peak}}$ is generic, but that the value of z_{peak} depends on assumptions about the characteristic gas consumption timescale, as parameterised by t_0^* . For plausible values of t_0^* we find that z_{peak} should be restricted to the range $3 \lesssim z_{\text{peak}} < 8.7$, with a firm upper limit corresponding to instantaneous gas consumption. In our numerical simulations, in which we chose t_0^* to reproduce the empirical Kennicutt Law, $z_{\text{peak}} \approx 5.5$.

Overall, we broadly predict that the cosmic star formation history in hierarchical universes should have a generic form, rising exponentially at first, peaking at z_{peak} , and then declining to $z = 0$ as a power-law function of $H(z)$. The logarithmic slopes on either side of the peak are mainly determined by cosmology, but the overall normalisation of $\dot{\rho}_*(z)$ and the value of z_{peak} are sensitive to assumptions about gas and star formation physics. The generic form we propose is compactly summarised by e.g. equation (2), where the value of β is fixed by cosmology and $\dot{\rho}_*(0)$ and α determine the overall normalisation and the location of z_{peak} .

We note that there are implicit assumptions in our description of the star formation physics that can influence e.g. α and z_{peak} in fits of the form of equation (2). For example, for simplicity we have assumed that cooling rates are those appropriate for a H/He plasma of primordial abundance. It is believed that at very high redshift, $z \sim 20 - 30$, molecular cooling is an important physical mechanism for early star formation (e.g. Bromm et al. 1999, Abel et al. 2002). Thus, our results are not applicable to Population III (e.g. Carr 1984) star formation and will not properly characterise $\dot{\rho}_*(z)$ until star formation globally resembles that at lower redshifts. How and when the Universe made this transition is uncertain. Simple estimates suggest that it may have occurred at $z \sim 15 - 20$, as the Universe began to become

chemically enriched (e.g. Mackey et al. 2002), but more detailed studies of this fundamental issue are clearly needed.

In our simulations, we have also ignored the contribution of metal line cooling to the overall cooling rate. However, we have been able to estimate the possible importance of this process using our analytical model, as described in Section 5.2. While our conclusions depend in detail on uncertainties in how efficiently enriched gas is mixed into galactic halos and the IGM, we find that metal line cooling does not affect our results at early times and likely has only a modest influence on the behaviour of $\dot{\rho}_*(z)$ at low redshift. In particular, if metals carried by galactic winds are efficiently mixed with the remaining gas in the universe, enhancements in the cooling and star formation rates at low redshift increase the stellar density only by $\sim 20 - 30\%$ by $z = 0$, boosting the star formation rate by a similar factor for $z \lesssim 3$. We note that when we previously compared our simulations to observations, there was an indication that our predicted $\dot{\rho}_*(z)$ was perhaps low at $z \sim 1$ (e.g. figure 12 in Springel & Hernquist 2002b). If we take this discrepancy seriously, given observational uncertainty, then metal cooling would boost the predicted star formation rate into the observed range, at least according to our present simple estimates, without violating constraints on the total stellar density at $z = 0$.

Metal enrichment can also, in principle, influence the location of z_{peak} and shift it to lower z . However, our current estimate of this effect suggests that the peak will still lie at a relatively high redshift, $z_{\text{peak}} \sim 5$, as indicated by Figure 13, and would thus not substantially alter our predictions for the evolution of the stellar density or the mean age of the stellar population with redshift. Furthermore, we do not believe that the overall form of the star formation history we considered here would be altered significantly. However, detailed hydrodynamical simulations of metal enrichment processes will ultimately be required to more accurately constrain the relevance of metal cooling for our modeling.

ACKNOWLEDGEMENTS

We thank Simon White for instructive discussions and critical comments that were helpful for the work on this paper. This work was supported in part by NSF grants ACI 96-19019, AST 98-02568, AST 99-00877, and AST 00-71019. The simulations were performed at the Center for Parallel Astrophysical Computing at the Harvard-Smithsonian Center for Astrophysics.

REFERENCES

- Abel T., Bryan G. L., Norman M. L., 2002, *Science*, 295, 93
 Ascasibar Y., Yepes G., Gottlöber S., Müller V., 2002, *A&A*, 387, 396
 Baldry I. K., Glazebrook K., Baugh C. M., et al., 2002, *ApJ*, 569, 582
 Balogh M. L., Pearce F. R., Bower R. G., Kay S. T., 2001, *MNRAS*, 326, 1228
 Baugh C. M., Cole S., Frenk C. S., Lacey C. S., 1998, *ApJ*, 498, 504
 Bromm V., Coppi P. S., Larson R. B., 1999, *ApJ*, 527, 5
 Bromm V., Loeb A., 2002, *ApJ*, 575, 111
 Carr B. J., Bond J. R., Arnett W. D., 1984, *ApJ*, 277, 445
 Cen R., Ostriker J. P., 1999, *ApJ*, 519, L109
 Cole S., Aragon-Salamanca A., Frenk C. S., Navarro J. F., Zepf S. E., 1994, *MNRAS*, 271, 781
 Cole S., Norberg P., Baugh C. M., et al., 2001, *MNRAS*, 326, 255
 Connolly A. J., Szalay A. S., Dickinson M., Subbarao M. U., Brunner R. J., 1997, *ApJ*, 486, L11
 Cowie L. L., Songaila A., Barger A. J., 1999, *ApJ*, 118, 603
 Cowie L. L., Songaila A., Hu E. M., Cohen J. G., 1996, *AJ*, 112, 839
 Davé R., Hernquist L., Katz N., Weinberg D. H., 1999, *ApJ*, 511, 521
 Davé R., Cen R., Ostriker J. P., et al., 2001, *ApJ*, 552, 473
 Flores H., Hammer F., Thuan T. X., et al., 1999, *ApJ*, 517, 148
 Fukugita M., Hogan C. J., Peebles P. J. E., 1998, *ApJ*, 503, 518
 Gallego J., Zamorano J., Aragon-Salamanca A., Rego M., 1995, *ApJ*, 455, L1
 Gradstein I. S., Ryzhik I. M., 1981, *Tables*, MIR Publishers, Moscow
 Gronwall C., 1999, in *After the Dark Ages: When galaxies were young*, edited by S. Holt, E. Smith, 335, Am. Inst. Phys. Press, Woodbury, NY
 Hogg D. W., 2001, preprint, astro-ph/0105280
 Hughes D. H., Serjeant S., Dunlop J., et al., 1998, *Nature*, 394, 241
 Jang-Condell H., Hernquist L., 2001, *ApJ*, 548, 68
 Jenkins A., Frenk C. S., White S. D. M., et al., 2001, *MNRAS*, 321, 372
 Kennicutt R. C., 1989, *ApJ*, 344, 685
 Kennicutt R. C., 1998, *ApJ*, 498, 541
 Lanzetta K. M., Yahata N., Pascarelle S., Chen H., Fernandez-Soto A., 2002, *ApJ*, 570, 492
 Lilly S. J., Fevre O. L., Hammer F., Crampton D., 1996, *ApJ*, 460, L1
 Mackey J., Bromm V., Hernquist L., 2002, preprint, astro-ph/0208447
 Madau P., Ferguson H. C., Dickinson M. E., Giavalisco M., Steidel C. C., Fruchter A., 1996, *MNRAS*, 283, 1388
 Madau P., Pozzetti L., Dickinson M., 1998, *ApJ*, 498, 106
 Nagamine K., Cen R., Ostriker J. P., 2000, *ApJ*, 541, 25
 Nagamine K., Fukugita M., Cen R., Ostriker J. P., 2001, *ApJ*, 558, 497
 Pascarelle S. M., Lanzetta K. M., Fernandez-Soto A., 1998, *ApJ*, 508, L1
 Pearce F. R., Jenkins A., Frenk C. S., et al., 2001, *MNRAS*, 326, 649
 Press W. H., Schechter P., 1974, *ApJ*, 187, 425
 Salpeter E. E., 1955, *ApJ*, 121, 161
 Sheth R. K., Tormen G., 1999, *MNRAS*, 308, 119
 Sheth R. K., Tormen G., 2002, *MNRAS*, 329, 61
 Somerville R. S., Primack J. R., Faber S. M., 2001, *MNRAS*, 320, 504
 Somerville R. S., Primack J. R., 1999, *MNRAS*, 310, 1087
 Springel V., Hernquist L., 2002a, preprint, astro-ph/0206393
 Springel V., Hernquist L., 2002b, preprint, astro-ph/0206395
 Springel V., Hernquist L., 2002c, *MNRAS*, 333, 649
 Springel V., White S. D. M., Tormen B., Kauffmann G., 2001, *MNRAS*, 328, 726
 Steidel C. C., Adelberger K. L., Giavalisco M., Dickinson M., Pettini M., 1999, *ApJ*, 519, 1
 Tresse L., Maddox S. J., 1998, *ApJ*, 495, 691
 Treyer M. A., Ellis R. S., Milliard B., Donas J., Bridges T. J., 1998, *MNRAS*, 300, 303
 Weinberg D. H., Davé R., Gardner J. P., Hernquist L., Katz N., 1999, in *Photometric Redshifts and the Detection of High Redshift Galaxies*, edited by R. Weymann, L. Storrie-Lombardi, M. Sawicki, R. Brunner, vol. 191, ASP Conference Series, 341
 White S. D. M., Frenk C. S., 1991, *ApJ*, 379, 52

- Wilson G., Cowie L. L., Barger A. J., Burke D. J., 2002, *AJ*, 124,
1258
Yoshida N., Stöhr F., Springel V., White S. D. M., 2002, *MNRAS*,
335, 762